Quantifying Isentropic Mixing Linked to Rossby Wave Breaking in a Modified Lagrangian Coordinate

CHENGJI LIU AND ELIZABETH A. BARNES

Department of Atmospheric Science, Colorado State University, Fort Collins, Colorado

(Manuscript received 11 July 2017, in final form 2 January 2018)

ABSTRACT

Isentropic mixing is an important process for the distribution of chemical constituents in the mid- to high latitudes. A modified Lagrangian framework is applied to quantify the mixing associated with two distinct types of Rossby wave breaking (i.e., cyclonic and anticyclonic). In idealized numerical simulations, cyclonic wave breaking (CWB) exhibits either comparable or stronger mixing than anticyclonic wave breaking (AWB). Although the frequencies of AWB and CWB both have robust relationships with the jet position, this asymmetry leads to CWB dominating mixing variability related to the jet shifting. In particular, when the jet shifts poleward the mixing strength decreases in areas of the midlatitude troposphere and also decreases on the poleward side of the jet. This is due to decreasing CWB occurrence with a poleward shift of the jet. Across the tropopause, equatorward of the jet, where AWB mostly occurs and CWB rarely occurs, the mixing strength increases as AWB occurs more frequently with a poleward shift of the jet. The dynamical relationship above is expected to be relevant both for internal climate variability, such as the El Niño–Southern Oscillation (ENSO) and the annular modes, and for future climate change that may drive changes in the jet position.

1. Introduction

Atmospheric transport and mixing play a fundamental role in the global distribution of chemical pollutants and moisture. In the extratropics, transport and mixing by eddies are known to mainly operate along isentropic surfaces [i.e., constant potential temperature (θ) surfaces]. Within the troposphere, warm conveyer belts embedded in extratropical cyclones transport warm moist air poleward and upward along sloped isentropes (e.g., Thorncroft et al. 1993; Madonna et al. 2014). These transport events are responsible for poleward moisture transport (e.g., Eckhardt et al. 2004) and pollutant transport into the Arctic (e.g., Raatz and Shaw 1984; Barrie 1986). In the upper troposphere, vigorous exchange between stratospheric and tropospheric constituents happens along isentropes across a folding tropopause (e.g., Shapiro 1980). Such exchange is an important source of ozone in the troposphere (e.g., Lelieveld and Dentener, 2000) where it is considered a pollutant and is detrimental to human health (e.g., Lippmann 1989). This exchange also injects anthropogenic trace species such as chlorofluorocarbon (CFC) into the stratosphere (Holton et al. 1995).

Because of the dominance of isentropic transport and mixing in the extratropics, θ is often used as the vertical coordinate in quantifying these processes. Under the adiabatic approximation, θ can be considered a material surface and, hence, a Lagrangian coordinate. A Lagrangian coordinate is a more natural choice than an Eulerian one for transport and mixing since it avoids the need for Stokes drift corrections arising from the Eulerian mean (McIntyre 1980). With θ being the vertical coordinate, reversible vertical oscillations are absent and any vertical flux is associated with diabatic heating. Along these same lines, it is natural to also choose a conserved variable as the meridional coordinate so that any meridional flux in such a coordinate is only associated with nonconservative processes, such as horizontal diffusion. Examples include using potential vorticity (PV) or the concentration of a passive tracer as the meridional coordinate (e.g., Butchart and Remsberg 1986). By integrating quantities between contours of a conserved quantity, a general description of the irreversible mixing is possible without expensive trajectory calculations (e.g., Nakamura 1995, 1996; Haynes and Shuckburgh 2000a).

As there are many ways to quantify isentropic mixing, there are many physical processes that drive them. Among them, Rossby wave breaking (RWB) is an

Corresponding author: Chengji Liu, cjliu@atmos.colostate.edu

DOI: 10.1175/JAS-D-17-0204.1

important one both within the troposphere and across the tropopause. Near the tropopause, RWB has been shown by numerous studies to be associated with the exchange of mass or chemical tracers between the stratosphere and the troposphere (e.g., Appenzeller and Davies 1992; Trepte et al. 1993; Chen 1995; Appenzeller et al. 1996; Jing et al. 2004). Especially strong exchange occurs in the presence of a double tropopause (e.g., Randel et al. 2007; Pan et al. 2009; Liu and Barnes 2018), which is a feature related to RWB (e.g., Wang and Polvani 2011; Liu and Barnes 2018). In the troposphere, we will show that RWB is also closely linked to isentropic mixing.

RWB can be classified into two distinct types—anticyclonic wave breaking (AWB) and cyclonic wave breaking (CWB)— and the frequency of each is strongly coupled to the midlatitude jet stream. Climatologically, AWB occurs most frequently on the equatorward flank of the jet where the horizontal wind shear is anticyclonic, while CWB occurs most frequently on the poleward flank of the jet. As the jet shifts poleward, the total frequency of AWB increases whereas that of CWB decreases (e.g., Strong and Magnusdottir 2008; Woollings et al. 2008; Rivière 2011; Barnes and Hartmann 2012). This RWB–jet position relationship is especially important because the jet stream position is very responsive to both internal climate variability, such as El Niño–Southern Oscillation (ENSO) (e.g., Rasmusson and Wallace 1983; Chen and Van den Dool 1999; Ren et al. 2008), and external climate forcings, such as increasing greenhouse gas concentrations and ozone depletion (e.g., Thompson and Solomon 2002; Butler et al. 2010; Barnes and Polvani 2013). It is through such coupling that RWB is linked to climate variability on different time scales, and thus, can drive the variability of global transport and mixing of various chemical tracers.

Quantifying the isentropic mixing by RWB is thus key to understanding the variability of the climate-scale distribution of various chemical tracers. Polvani and Esler (2007, hereafter PE07) quantified the two-way mixing across the tropopause associated with the two types of RWB in idealized eddy life cycle simulations. They found that CWB exhibits stronger mixing from the stratosphere to the troposphere compared to AWB. Considering the coupling of the jet stream position and AWB versus CWB frequency, such a difference has significant implications since it may translate into a change in total mixing when the jet stream shifts. In this work, we explore these implications by asking two questions: 1) Is there a robust asymmetry in isentropic mixing efficiency between AWB and CWB? 2) How does this asymmetry, if it exists, translate into a dependence of total mixing on jet variability?

The paper is organized as follows. A description of the numerical simulations is given in section 2. In section 3, we describe a modified Lagrangian framework to quantify isentropic mixing. Section 4 explores mixing linked to both types of RWB, and tests the robustness of the difference between AWB and CWB. Section 5 shows how such difference can impact total mixing as the jet stream shifts. Conclusions are given in section 6.

2. Model setups

All simulations in this study are performed by integrating a primitive equation model with no topography. The specific model used is the Geophysical Fluid Dynamics Laboratory (GFDL) spectral dry dynamical core. We carried out simulations with a horizontal resolution of both T42 and T85, and found most of our results to be robust regardless of the resolution. All the figures below show the results from the higher resolution (T85). The model uses ∇^8 horizontal hyperdiffusion for dynamical variables such as temperature, vorticity, and divergence. There is no explicit vertical diffusion for any variable in this model.

With the same model setup described above, we carry out two different sets of simulations. The first set of simulations are idealized eddy life cycle simulations with initialized passive tracers that follow PE07 (to be discussed in detail). The second simulation is an idealized climate run based on Held and Suarez (1994). The focus of this study is the results from the climate simulation, with those from the life cycle simulations mainly for comparison.

a. Idealized eddy life cycle simulation

Following PE07, we reproduce the two idealized eddy life cycles (LC1 and LC2) first introduced by Thorncroft et al. (1993). The model is configured with 60 unevenly spaced vertical layers and no diabatic heating during the 20-day run. In both the LC1 and LC2 simulations, only the initial conditions are prescribed. For LC1, a baroclinically unstable jet is prescribed at initialization and the eddies grow and break anticyclonically at the late stages of the life cycle, which corresponds to AWB in the real atmosphere. The initial zonal wind is given by

$$u_1(\phi, z) = U_0 F(\phi)\{(z/z_T)\, e^{-[(z/z_T)^2-1]/2}\}\,, \tag{1a}$$

$$F(\phi) = \begin{cases} \left\{\sin[\pi(\sin\phi)^2]\right\}^3, & \text{for } \phi > 0 \\ 0, & \text{for } \phi < 0 \end{cases}, \tag{1b}$$

where $z = H\log(p_0/p)$ is the log-pressure height. For LC2, the initial zonal wind is obtained by adding a bottom-heavy cyclonic shear u_s to the initial wind profile for LC1:

$$u_2(\phi, z) = u_1(\phi, z) + u_s(\phi, z), \tag{2a}$$

$$u_s(\phi, z) = -U_s\, e^{-z/z_s}[\sin(2\phi)]^2 \left(\frac{\phi - \phi_s}{\Delta_s}\right) e^{-\left(\frac{\phi-\phi_s}{\Delta_s}\right)^2}. \tag{2b}$$

In the LC2 simulation the eddies grow and break cyclonically at the late stages of the life cycle, which corresponds to CWB. The constants appearing in (1) and (2) are the same as those in PE07. For example, the jet strength $U_0 = 45\,\mathrm{m\,s^{-1}}$ and the scale height (z_s) and location (ϕ_s) for the wind shear added to LC2 are 10 km and 35°N, respectively. For both life cycles, the initial conditions for temperature and surface pressure are set to be in thermal wind balance with the zonal wind profiles prescribed in (1) and (2). In addition to the balanced temperature profile, a wavenumber-6 perturbation centered at 45°N is added to the initial temperature field to give rise to the growing eddies.

For both the LC1 and LC2 simulations, the tracer setup is similar to PE07 in that we initialize two passive isentropic tracers: a stratospheric tracer (S) and a tropospheric tracer (T) on isentropes ranging from 290 to 380 K. The initial tropopause is defined (as in PE07) as a nearly vertical boundary that partitions isentropes into a poleward half (stratosphere) and a equatorward half (troposphere) (see Fig. 5 in PE07). The initial concentrations of the two tracers are set such that poleward of the initial tropopause $S = 1$ and $T = 0$, while equatorward of it $T = 1$ and $S = 0$. Since the simulations are adiabatic, $S + T = 1$ on isentropes from 290 to 380 K at all times by construction. During the simulations, the tropopause is defined by an evolving boundary between the two tracers as the contour of $S = T = 0.5$. Both S and T are spectral tracers and a ∇^8 hyperdiffusion is applied at each time step. We refer readers to PE07 for additional details.

b. Idealized climate simulation

We perform a climate simulation forced by the idealized diabatic heating scheme proposed by Held and Suarez (1994). Specifically, we set the diabatic heating as a relaxation to a prescribed zonally symmetric equilibrium temperature profile:

$$T_{\mathrm{eq}} = \max\left\{200\,\mathrm{K}, \left[315\,\mathrm{K} \underbrace{-(\Delta T)_y \sin^2\phi}_{\mathrm{A}} \underbrace{-(\Delta\theta)_z \log(p/p_0)\cos^2\phi}_{\mathrm{B}} \underbrace{-\varepsilon\sin\phi}_{\mathrm{C}}\right] \underbrace{(p/p_0)^\kappa}_{\mathrm{D}}\right\}. \tag{3}$$

For this relaxation scheme, the individual terms in (3) are equivalent to constant heating or cooling terms. Idealized as it is, (3) includes the most essential elements of climate forcing— heating in low latitudes and cooling in high latitudes—as represented by term A. Term B is a modification for the tropics, as manifested by the $\cos^2\phi$ factor. Without term B, but with the inclusion of factor D, (3) would yield an atmosphere that was stratified dry adiabatically. Term B thus can be thought of as a representation of stabilization by moist convection in the tropics, which is not represented explicitly in this model setup. Term C adds a hemispheric asymmetry to the equilibrium temperature that accounts for seasonality in radiative forcing. In this study we set $\varepsilon = 10$, which represents winter conditions in the Northern Hemisphere. We focus on winter because the eddy activity is strongest in winter when the baroclinicity is largest. In addition, the low-frequency variability that modulates eddy activity (e.g., the annular mode) is also strongest in the winter.

While the equilibrium temperature profile given in (3) leads to a midlatitude circulation that is generally representative of that which is observed, there are still noticeable differences, especially in the tropics. For example, the Hadley cell in this dry general circulation model (GCM) is substantially weaker than in observations (e.g., Walker and Schneider 2006). However, the main purpose of this simulation is not to reproduce the observed circulation exactly (e.g., there is no topography), but to serve as a stepping stone between the unforced eddy life cycle simulation and reality by removing the complexities of full GCMs that are not essential for isentropic mixing.

To study isentropic mixing, we initialize a spectral tracer that serves as our Lagrangian coordinate. As will be explained in the next section, the tracer is required to 1) have a monotonic meridional gradient and 2) be passive. To satisfy the first requirement the tracer has a source and a sink in the boundaries of the domain and to satisfy the second requirement the quantification of mixing is only done away from the boundaries where the tracer is purely passive. The source of the tracer can be thought of as sitting in the surface boundary layer from 60°S to 60°N and the sink includes the entire free

atmospheric column poleward of 85°N and 85°S. In the sink region the tracer concentration is damped exponentially with an *e*-folding time scale of 6 h. In the source region within the surface boundary layer, the tracer concentration is set at every time step to

$$\frac{1}{4.5}[3.7 - P_2(\sin\phi) - P_4(\sin\phi)], \tag{4}$$

where P_2 and P_4 are the second- and fourth-order Legendre polynomials, respectively. Equation (4) is qualitatively similar to a tracer concentration of 1 from 60°S to 60°N and 0 elsewhere in the surface boundary layer, but with a gradual transition from 1 to 0 on the edges, which prevents spurious tracer concentration during integration because of the Gibbs effect. The tracer is otherwise passive throughout the rest of the atmosphere. As in the life cycle simulations, a ∇^8 hyperdiffusion is used for the spectral tracer.

With the setup described above, the model is run with 40 evenly spaced sigma levels for 25 years. We use the last 22 yr for analysis, which allows for a spinup period of about 1000 days. All of the variables are out put every 6 h.

3. Quantification of isentropic mixing

a. *Modified-Lagrangian-mean framework and the tracer equation*

Viewed in an Eulerian framework, the distribution of a passive tracer can be accounted for by two processes: advective fluxes and diffusive fluxes. The idea of a modified Lagrangian coordinate is to reformulate the Eulerian tracer equation in a flow-following two-dimensional coordinate so that reversible advective fluxes are absent. Specifically, we can choose potential temperature (θ) as the vertical coordinate, and the concentration of a passive tracer (q) as the meridional coordinate. As shown by Nakamura (1995), under such a coordinate transformation, the mass continuity equation becomes

$$\left.\frac{\partial \mathscr{M}\{1\}}{\partial t}\right|_{q,\theta} = -\left.\frac{\partial \mathscr{M}\{\dot{q}\}}{\partial q}\right|_{\theta,t} - \left.\frac{\partial \mathscr{M}\{\dot{\theta}\}}{\partial \theta}\right|_{q,t}, \tag{5}$$

where $\dot{q}$ and $\dot{\theta}$ are the material derivatives of q and θ, and

$$\mathscr{M}\{\,\} \equiv \iint_{q^* \le q} \{\,\}\sigma\, dA \tag{6}$$

in which $\sigma \equiv -g^{-1}\partial p/\partial\theta$ is the pseudodensity in isentropic coordinates and q^* denotes the tracer concentration within the integration area. Note that in the climate simulation q decreases with latitude as determined by the sources and sinks of our passive tracer. On the lhs of (5) is the mass tendency within a contour of q. The first term on the rhs of (5) accounts for horizontal transport of mass across a contour of q caused by diffusion, while the second term represents the differential vertical transport of mass across isentropic surfaces caused by diabatic heating.

To obtain a tracer equation from (5), we largely follow Nakamura (1996) except that we utilize the one-to-one relationship between a tracer contour q and the *mass* enclosed by it $m = \mathscr{M}\{1\}$, rather than the *area* enclosed. In particular, on each isentrope one can obtain the following relationship between q and m by taking the total derivative of the time invariant coordinate quantity $m(q, t)$:

$$\frac{dm(q,t)}{dt} = \left.\frac{\partial m}{\partial t}\right|_q + \left.\frac{\partial m}{\partial q}\frac{\partial q}{\partial t}\right|_m = 0. \tag{7}$$

Plugging (7) into (5) leads to the tracer equation in the mass coordinate:

$$\left.\frac{\partial q}{\partial t}\right|_{m,\theta} = \left.\frac{\partial \mathscr{M}\{\dot{q}\}}{\partial m}\right|_{\theta,t} + \left.\frac{\partial q}{\partial m}\frac{\partial \mathscr{M}\{\dot{\theta}\}}{\partial \theta}\right|_{q,t}. \tag{8}$$

Note that this is equivalent to the tracer equation used in Leibensperger and Plumb (2014) but without further coordinate transformation. On the lhs is the time tendency of the value of a tracer contour that encloses a fixed mass m. The first term on the rhs is the convergence of diffusive tracer flux, which is downgradient in general. The second term represents the contribution of diabatic mass circulation and is analogous to "advection" if $\partial\mathscr{M}\{\dot{\theta}\}/\partial\theta\,|_{q,t}$ is taken as the "meridional" velocity (Leibensperger and Plumb 2014).

In the case of nondivergent barotropic flow ($\sigma = \sigma_0$), the second term on the rhs of (8) vanishes. The diffusive term $\mathscr{M}\{\dot{q}\}$ then accounts for the tracer distribution alone and is the one closely linked to Rossby wave breaking (to be shown later). In this study, we focus on this diffusive term not only because of its linkage to wave breaking, but also because of its dominance in the midlatitudes in determining zonally averaged tracer distributions (e.g., Plumb and Mahlman 1987).

The diffusive nature of term $\mathscr{M}\{\dot{q}\}$ can be revealed by such a flux–gradient relationship assuming $\dot{q} = \kappa\nabla_\theta^2 q$ (Nakamura 1996):

$$\mathscr{M}\{\dot{q}\} = \sigma_0 \kappa L_{\mathrm{eq}}^2\, \partial q/\partial A, \tag{9}$$

where $A(q, \theta, t)$ is the area enclosed by a contour q, and

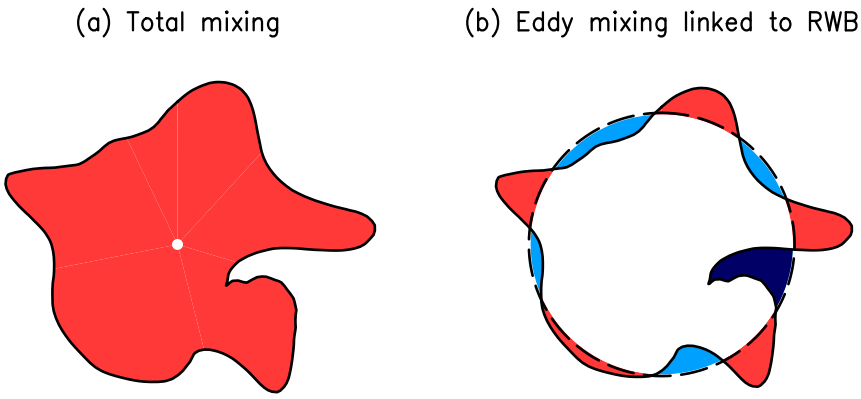

FIG. 1. Schematics depicting the integration area for (a) total mixing and (b) eddy mixing by waves (all shading), along with the part related to Rossby wave breaking (dark blue shading). See text for additional details.

$$L_{\rm eq}^2 = \frac{\partial}{\partial A}\iint |\nabla_\theta q|^2\, dA/(\partial q/\partial A)^2. \tag{10}$$

Note ∇_θ denotes the horizontal gradient on isentropes (θ). The quantity $L_{\rm eq}$ is called equivalent length and leads to the definition of effective diffusivity (Haynes and Shuckburgh 2000a):

$$\kappa_{\rm eff} = \kappa \frac{L_{\rm eq}^2}{(2\pi a\cos\phi)^2}. \tag{11}$$

We refer readers to the appendix for the derivation of (9). Since $L_{\rm eq}^2$ is positive definite, the sign of flux $\mathscr{M}\{\dot{q}\}$ is downgradient in this instance. In other words, $\mathscr{M}\{\dot{q}\}$ is diffusive in nature. By construction, $L_{\rm eq}^2$ cannot be less than $(2\pi a\cos\phi)^2$ so the effective diffusivity $\kappa_{\rm eff}$ has a lower bound of κ. In reality, the large-scale stirring can make $\kappa_{\rm eff}$ much larger than κ.

b. Calculation of the isentropic diffusivity

To calculate the diffusive flux term in (8), we need to first determine the mass values to use as coordinates. For both idealized eddy life cycle simulations and the climate simulation, we pick 60 values of m for each isentropic level in the Northern Hemisphere by their one-to-one relationship with equivalent latitude ϕ_e:

$$m(\phi_e) = \iint_{\phi\ge\phi_e} \overline{\sigma}\, dS, \tag{12}$$

where $\overline{\sigma}$ is the climatological-mean pseudodensity. Specifically, we first evenly pick 60 ϕ_e values ranging from 0° to 85°N and then obtain 60 corresponding m from (12).

The diffusive flux $\mathcal{M}\{\dot{q}\}$ in (8) is then calculated as area integral of $\sigma\dot{q}$ at each $\phi_e(m)$. The quantity $\dot{q}$ is calculated as the fourth-order hyperdiffusion in the model, and we output $\dot{q}$ at 6-hourly intervals and interpolate it and σ on isentropic surfaces following the interpolation scheme of Edouard et al. (1997). The integration area for $\mathscr{M}\{\dot{q}\}$ is illustrated in Fig. 1a. For the climate simulation, we are especially interested in mixing driven by eddies. To serve this purpose, we partition the integration of $\mathscr{M}\{\dot{q}\}$ into two parts following previous studies (e.g., Nakamura and Zhu 2010; Chen and Plumb 2014):

$$\mathscr{M}\{\dot{q}\} = \overline{\mathscr{M}}\{\dot{q}\} + \Delta\mathscr{M}\{\dot{q}\}. \tag{13}$$

The first term is $\overline{\mathscr{M}}\{\dot{q}\}$ that represents the integration poleward of an equivalent latitude circle (ϕ_e). The integration area for this term is indicated by the black dashed circle in Fig. 1b. This term is driven only by diffusion. The second term is $\Delta\mathscr{M}\{\dot{q}\}$ that is driven by zonal asymmetries in the flow (i.e., eddies). Specifically,

$$\Delta\mathscr{M}\{\dot{q}\} = \iint_{q^*>q,\phi>\phi_e} \dot{q}\sigma\, dS - \iint_{q^*<q,\phi<\phi_e} \dot{q}\sigma\, dS. \tag{14}$$

The integration area in (14) is indicated by the shading in Fig. 1b where the red and blue areas corresponds to the first and second terms on the rhs of (14), respectively. The term $\Delta\mathscr{M}\{\dot{q}\}$ (from now on referred to as eddy mixing) is the component we focus on here.

As suggested by (9), eddy mixing flux $\Delta\mathscr{M}\{\dot{q}\}$ is determined by both dynamics (diffusivity) and specific tracer distributions (tracer gradient). We are only interested in the more general dynamical part since its behavior is transferable to any other tracer. This part is referred to as effective eddy diffusivity and can be calculated as $\Delta\mathscr{M}\{\dot{q}\}$ normalized by the tracer gradient and mean mass density suggested by (9) and (11), that is,

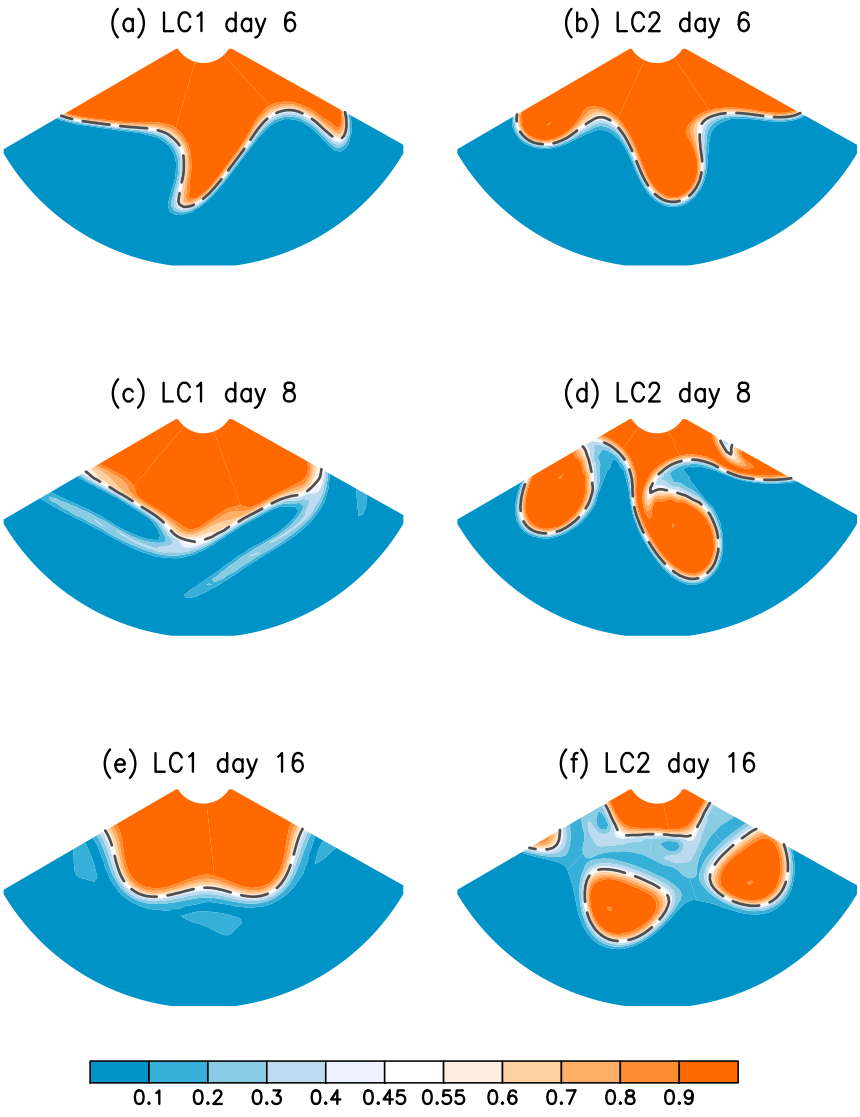

FIG. 2. Snapshots of the concentration of the stratospheric tracer (shading) on the 335-K isentrope in the idealized (left) LC1 and (right) LC2 simulations: day (top) 6, (middle) 8, and (bottom) 16. Dashed contours denote the tropopause defined as the 0.5 contour of the stratospheric tracer.

$\Delta\mathscr{M}\{\dot{q}\}/(\overline{\sigma}^L\,\partial q/\partial\phi_e)$, where $\overline{\sigma}^L$ is the climatological mean of the average pseudodensity over a tracer contour. Note that this expression of eddy diffusivity is very similar to that of Chen and Plumb (2014). The main difference is that they employ a hybrid Eulerian–Lagrangian coordinate whereas we use a Lagrangian coordinate to be consistent with the quantification of the other quantities in our framework. In the rest of the paper, we use this eddy diffusivity to represent isentropic mixing strength.

c. *Linking isentropic mixing to Rossby wave breaking*

In this study, we separate mixing by the overturning direction of Rossby wave breaking—anticyclonic and cyclonic—because of the robust dynamical relationship between the two types of wave breaking and the jet streams (e.g., Barnes and Hartmann 2012). Note that Nakamura (2004) separates mixing into a poleward and an equatorward component. Since cyclonic and anticyclonic wave breaking events comprise a combination of poleward and equatorward mixing, our approach is distinct from this earlier work. For our idealized life cycle simulations, linking isentropic mixing to the two types of wave breaking is straightforward. As in PE07, we assume all of the mixing in the LC1 simulation is linked to AWB while all of the mixing in the LC2 is linked to CWB. However, for the climate simulation in which AWB and CWB coexist every day along with

other nonbreaking waves, we need a dedicated algorithm to separate the contribution from the two types of wave breaking from all of the other processes. To serve this purpose, we first detect the two types of RWB in the model output. Unlike some previous studies where contours of PV on isentropes are used to identify wave breaking events (e.g., Strong and Magnusdottir 2008; Liu et al. 2014; Liu and Barnes 2015), we base our algorithm on the tracer contours themselves. In fact, the contours of the tracer q in our climate simulation align well with PV contours on isentropic surfaces and thus our method is very similar to that of previous studies (not shown). The reason we favor q over PV for RWB detection is that our quantification of the mixing is based on q contours already. Thus, using q to detect RWB is natural for linking mixing to RWB events in this framework.

Specifically, we detect RWB based on wave lobes illustrated in Fig. 1b as red and blue patches. For each wave lobe, where it is attached to the equivalent latitude is called the "base line" of the lobe (shown as black dashed arcs in Fig. 1b). If the westmost–eastmost point of one lobe is to the west–east of its base line, then we identify the lobe as overturning. We require the extent of overturning be at least 5.5° of longitude to exclude small-scale disturbances that are not linked to large-scale RWB. Then, according to the direction of overturning, we partition the overturning lobes into AWB and CWB. For example, in Fig. 1b the overturning lobe is identified as CWB and marked by dark blue shading. The eddy mixing $\Delta\mathcal{M}\{\dot{q}\}$ associated with this CWB lobe is the integration over the dark blue area in Fig. 1b. The eddy mixing flux associated with RWB is normalized by the total tracer gradient to define the eddy diffusivity linked to RWB. The frequency of occurrence of RWB is defined as the ratio of RWB area to the total wave area (e.g., dark blue vs all shading in Fig. 1b). We compared the climatology of RWB frequency obtained by this method with that obtained by an algorithm using PV contours (Liu et al. 2014; Liu and Barnes 2015). They agree well with each other (not shown), thus further supporting our use of q contours for identifying RWB in this study.

A caveat should be raised about local RWB contribution to isentropic mixing. Since the divergence theorem does not hold for local integration, (9) does not necessarily hold for the RWB contribution (see the appendix for details). In other words, the local contribution to mixing is not guaranteed to be downgradient although the total mixing is, provided that the diffusion takes the form of $\dot{q} = \kappa\nabla_\theta^2 q$.

4. Isentropic mixing linked to the two types of Rossby wave breaking

Figure 2 illustrates distinct mixing features associated with the two types of Rossby wave breaking by showing

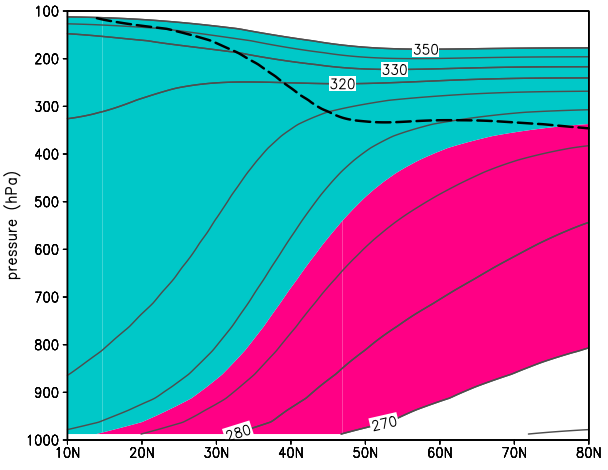

FIG. 3. Climatology of zonal-mean potential temperature θ in the 25-yr climate run (solid contours with an interval of 10 K). The dashed line denotes the climatological 2-PVU surface, which represents the dynamical tropopause. Pink and light green shading denote the underworld and the middleworld analyzed here, respectively.

snapshots of tracer S on the 335-K isentrope in the two idealized wave breaking simulations. Orange indicates the stratosphere and blue indicates the troposphere. On day 8, the anticyclonic overturning in LC1 is depicted by the blue shading equatorward of the tropopause (denoted by the black dashed line), and the cyclonic overturning in LC2 is depicted by orange shading poleward of the tropopause (Figs. 2c and 2d, respectively). It is evident in Figs. 2c and 2d that CWB in LC2 is much more active in stretching and overturning the tropopause (dashed line) compared to AWB in LC1. As a result, there is a larger interface between the S and T tracers for mixing to work on for CWB. Consistent with this picture, PE07 documented 50% stronger stratosphere-to-troposphere mixing in LC2 than in LC1.

Our goal for this section is to paint a more comprehensive picture for the mixing features linked to the two types of wave breaking provided by a more realistic climate simulation. By applying a wave breaking detection algorithm and modified-Lagrangian-mean diagnostic for mixing, we investigate the spatial distribution and efficiency of RWB-driven mixing on isentropes ranging from the troposphere to the lower stratosphere.

Figure 3 shows the climatology of isentropes (solid line) in pressure coordinates from the idealized climate simulation. The shading denotes the range of isentropes (270–350 K) on which we quantify mixing of the idealized tracer. We further divide the shaded area into the middleworld (green shading, 300–350 K) and the underworld (pink shading, 270–295 K) (e.g., Shaw and Austin 1930; Hoskins 1991). The underworld is defined by isentropes that are always below the tropopause denoted

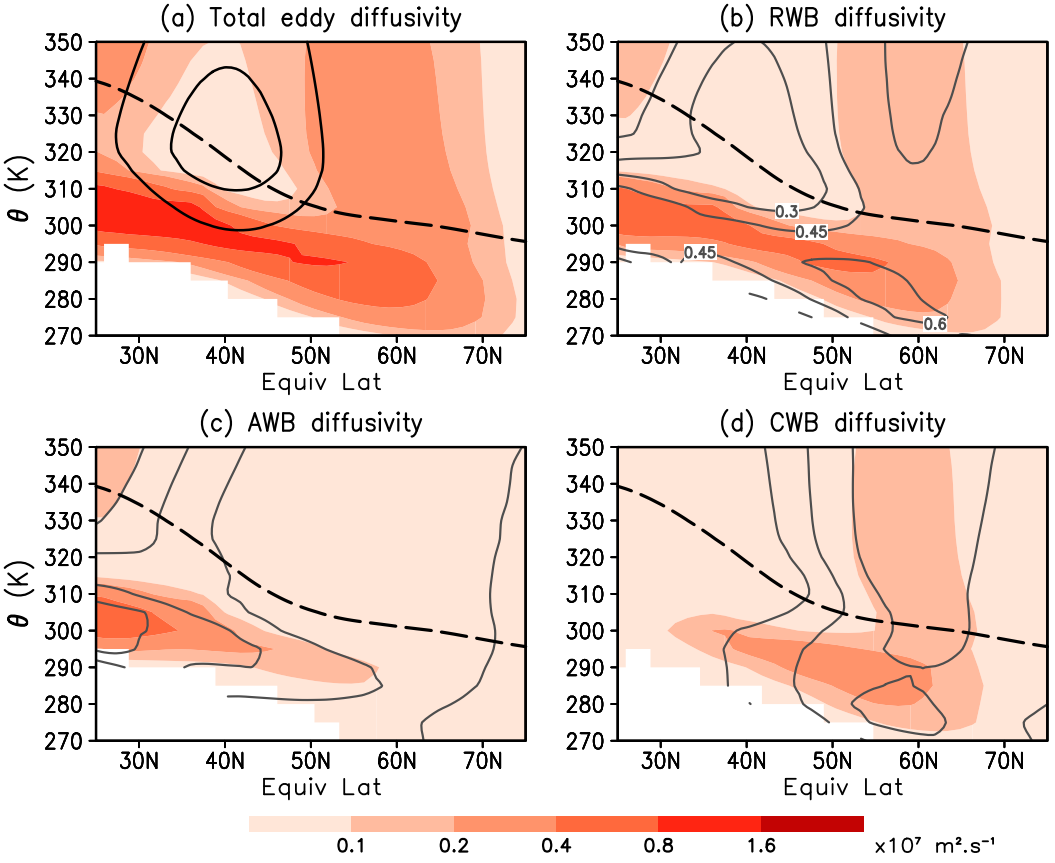

FIG. 4. Climatology of eddy diffusivity (shading) for the (a) total, (b) RWB contribution, (c) AWB contribution, and (d) CWB contribution. The two solid black contours in (a) denote the 20 and 30 m s^{-1} contours of the zonal-mean zonal wind. Contours in (b)–(d) denote the frequency of occurrence of RWB, AWB, and CWB events with a contour interval of 0.15, respectively. The black dashed lines are the 2-PVU contour that represents the dynamical tropopause.

by the 2-PVU contour (black dashed line; 1 PVU = 10^{-6} K kg^{-1} m^2 s^{-1}), while the middleworld is defined by isentropes that cross the tropopause. In the rest of the paper, the majority of the results are shown on these isentropes or as an average over the underworld or the middleworld.

The spatial pattern of the climatological eddy diffusivity is shown in Fig. 4a along with the jet stream (black solid contour). In Fig. 4a, eddy diffusivity has a local minimum at the jet core near the tropopause, indicating that jet acts as a mixing barrier in the middleworld (e.g., Haynes and Shuckburgh 2000b; Chen and Plumb 2014). The eddy diffusivity linked to RWB bears a very similar spatial pattern to the total (Fig. 4b), and in this model about 50% of the eddy mixing is done by large-scale RWB. The RWB frequency of occurrence is plotted in gray in Fig. 4b, and agrees well with the magnitude of the eddy diffusivity. This agreement confirms the dominant role of RWB in determining midlatitude eddy diffusivity.

The RWB contribution to eddy diffusivity is further divided into AWB contribution and CWB contribution shown in Figs. 4c,d (shading), along with their corresponding frequency of occurrence (gray contours). Overall, the contribution of AWB and CWB to eddy diffusivity is very well coupled to their frequency of occurrence. In particular, AWB mainly occurs at lower latitudes equatorward of the jet and so does the eddy diffusivity linked to it (Fig. 4c). CWB mainly occurs at higher latitudes poleward of the jet and so does the eddy diffusivity linked to it (Fig. 4d). In the middleworld, there is a clear separation between the occurrence of the two types of wave breaking. Therefore, there exists a region with minimum wave breaking frequency that also exhibits a minimum in wave breaking mixing strength (Fig. 4b). In the underworld, however, there is substantial overlap between the two types of wave breaking (Figs. 4c,d) and the total wave breaking frequency stays relatively constant across the entire mid- to high latitudes (Fig. 4b). Correspondingly, the total eddy

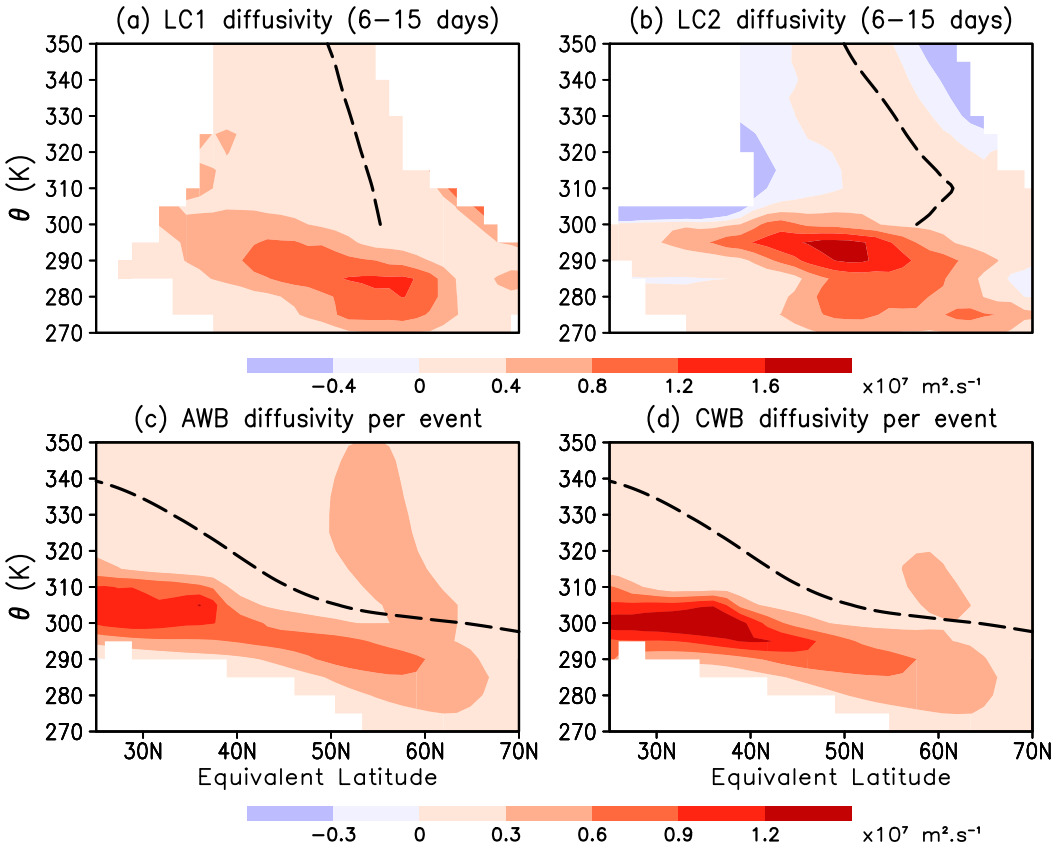

FIG. 5. (top) Eddy diffusivity (color shading) in the idealized life cycle simulations averaged over days 6–15 for (a) LC1 and (b) LC2. The dashed black lines denote the tropopause defined by where $T = S = 0.5$. (bottom) Climatology of eddy diffusivity in the 25-yr climate simulation for (c) AWB and (d) CWB, normalized by their respective frequency of occurrence. The black dashed lines denote the tropopause defined by where PV = 2 PVU.

diffusivity in the underworld does not exhibit a minimum near 40°N where zonal wind is strongest. (Figs. 4a,b)

A true comparison of the eddy diffusivity between the two types of RWB can be obtained by dividing their climatological-mean values by the frequency of RWB occurrence. Through this normalization, we factor out the contribution of frequency and compare the eddy diffusivity per occurrence of AWB/CWB (i.e., their mixing efficiency). Figures 5c,d compare the mixing efficiency of the two types of RWB in the climate simulation, along with their counterparts in the idealized eddy life cycle simulations shown in Figs. 5a,b. Note that areas with tracer $T \geq 0.99$ or $T \leq 0.01$ are masked out in Figs. 5a,b where the gradient of T is close to zero and eddy diffusivity becomes unrealistically large. In both the life cycle and climate simulations, CWB (LC2) exhibits a larger diffusivity than AWB (LC1) in the midlatitude underworld. The difference is evident in the majority of midlatitudes from 25° to 45°N equivalent latitude. Recall that the life cycle simulations are only made of one event, while the climate simulation comprises thousands. Thus, we do not expect the results to be identical. However, the life cycle simulations bear some resemblance to the climate simulations in Fig. 5, especially the relative difference in the magnitude of mixing efficiency between AWB and CWB. This indicates the relevance of the idealized life cycle simulations to more realistic climate settings.

Section summary

We quantify the climatology of isentropic mixing linked to the two types of RWB and find,

- In both idealized eddy life cycle simulations and a long climate simulation, CWB has stronger mixing efficiency (eddy diffusivity per event) than AWB in the underworld.
- The mixing efficiency in life cycle simulations bears resemblance to that in the climate simulations.

In the next section, we show how such asymmetry in RWB mixing efficiency translates into a dependence of total isentropic mixing on jet variability.

5. Dependence on jet stream variability

The dependence of isentropic mixing strength on the internal variability of the jet, specifically the latitudinal shifts of jet, is explored by compositing the eddy diffusivity with respect to various jet latitudes. We calculate the jet latitude as the latitude of maximum 850-hPa zonal-mean zonal wind at 6-h resolution (e.g., Barnes and Hartmann 2010; Woollings et al. 2010). We group the jet latitudes into four bins centered at 32°, 36°, 42°, and 48°N, and then composite RWB frequency, eddy diffusivity, and the contribution by RWB according to these jet latitude bins. Note that the binning is based on 6-hourly instantaneous jet locations without filtering, so we include the meridional fluctuation of the jet occurring on various time scales determined by the internal dynamics of the model.

a. Tropospheric mixing

The tropospheric isentropic mixing is investigated by focusing on the upper underworld (285–295 K), which constitutes a corridor between the subtropical boundary layer and the polar mid- to upper troposphere (Fig. 3). The average frequency of RWB in this corridor is shown in Fig. 6 as a function of equivalent latitude. Consistent with previous studies, AWB occurs more frequently while CWB occurs less frequently as the jet shifts poleward (e.g., Strong and Magnusdottir 2008; Woollings et al. 2008; Rivière 2011; Barnes and Hartmann 2012). The extent of the frequency change associated with AWB and CWB are comparable in midlatitudes around 45°N, indicating a compensation between the two types of RWB. Thus, total RWB frequency remains largely unchanged in the midlatitude as the jet shifts (Fig. 6c). The mixing efficiency related to CWB stays largely unchanged and that related to AWB exhibits a poleward shift as the jet shifts poleward (not shown). The fractional changes of these efficiencies are much smaller than those of the RWB frequencies and thus the changes in AWB- and CWB-related eddy diffusivity linked to the jet shifting (Figs. 7c,d) are dominated by their frequency changes (Figs. 6a,b).

Figures 7a and 7b show the total eddy diffusivity and the contribution from RWB for different jet positions. RWB contributes approximately half of the total. Both the total and RWB contribution to eddy diffusivity exhibit a poleward shift in pattern and a decrease in magnitude when the jet is more poleward. The substantial decrease in magnitude is mainly because CWB has a significantly larger eddy diffusivity than AWB (Figs. 5c and 5d). As a result, the decrease in CWB diffusivity caused by decreasing CWB frequency overwhelms the increase in AWB diffusivity caused by increasing AWB frequency (Figs. 7c,d), leading to decreased RWB diffusivity despite unchanged RWB

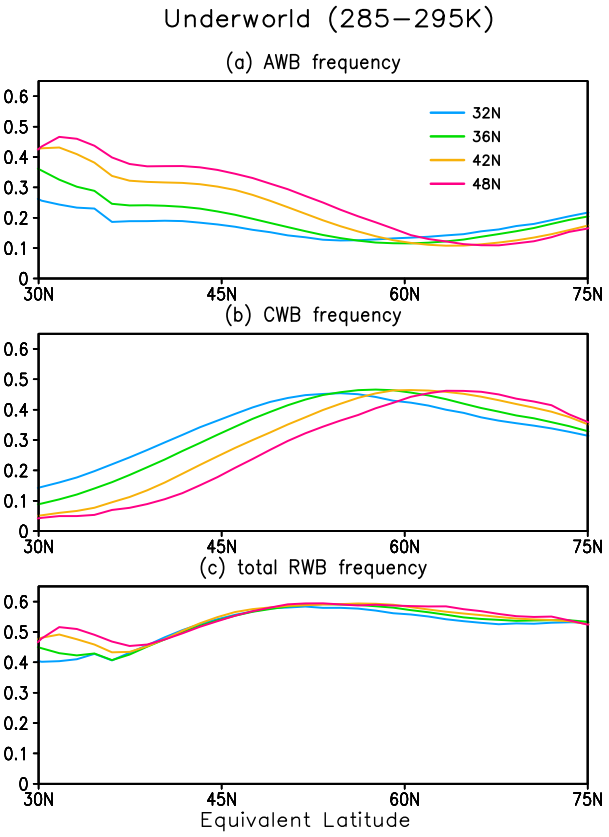

FIG. 6. Composite frequency of occurrence of RWB with respect to various jet positions for (a) AWB, (b) CWB, and (c) the total RWB in the upper underworld (285–295 K). The jet latitudes are denoted in the legend in (a).

frequency in the midlatitude (Fig. 6c). This effect is most evident in the midlatitudes between 30° and 55°N equivalent latitude. In this case, the difference between AWB and CWB mixing efficiency is key to determining the change in total eddy diffusivity linked with changes in the jet position.

b. Stratosphere–troposphere exchange (STE)

As shown in Fig. 2, RWB promotes STE by distorting the tropopause. The vertical distortion of the tropopause by AWB and CWB in the idealized life cycle simulations is demonstrated in Fig. 8 as snapshots on day 6 and day 7, respectively. The two dates are chosen based on the peak stage of AWB and CWB mixing. As in Fig. 2, orange denotes stratospheric air and blue indicates tropospheric air. Both AWB and CWB are associated with an intrusion of stratospheric air that extends to the middle troposphere. Around the intrusion, there exists a mixing area where both stratospheric air is mixed into the troposphere (light blue) and tropospheric air is mixed into the stratosphere (light orange). These streamers are also

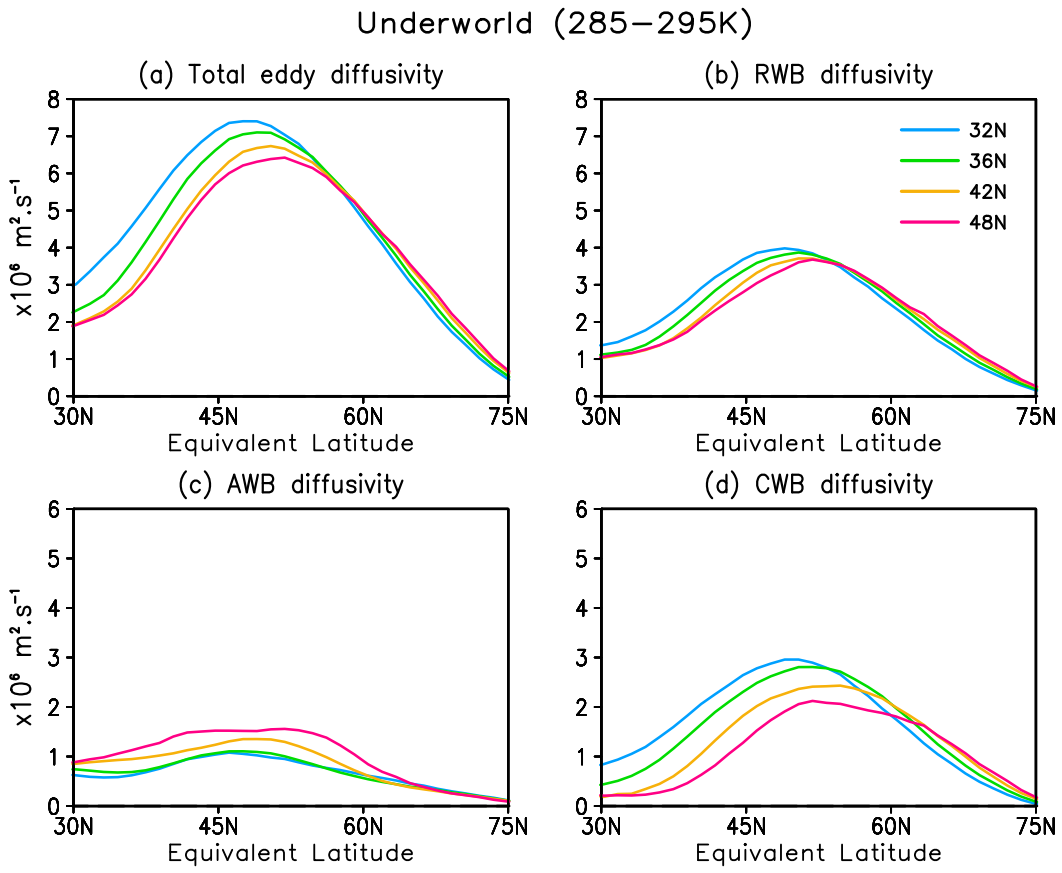

FIG. 7. Composite eddy diffusivity ($1 \times 10^6\ m^2\ s^{-1}$) in the upper underworld with respect to various jet positions for the (a) total, (b) RWB, (c) AWB, and (d) CWB. The jet latitudes are denoted in the legend in (b).

prevalent in nature (e.g., Shapiro 1980) and the two-way exchange across the tropopause was supported by Lagrangian trajectory studies (e.g., Sprenger and Wernli 2003; Škerlak et al. 2014). Quantifying the variability of RWB-related two-way STE as shown in Fig. 8 is, hence, of great interest. To serve this purpose, we first define the tropopause in the conventional (ϕ, θ) plane as where the zonal-mean climatological PV equals 2 PVU, giving us a relationship between θ and ϕ on the tropopause, $\theta_{TP}(\phi)$. Then, we apply this relationship directly to the modified Lagrangian coordinate, replacing ϕ with equivalent latitude ϕ_e. Namely, for any ϕ_e, the tropopause is defined on the isentrope $\theta_{TP}(\phi_e)$.

Following the same line of thought as that for tropospheric mixing, we assume the variability of stratosphere–troposphere exchange is also mainly determined by mixing efficiency and frequency of the two types of RWB. We begin by looking at the mixing efficiency. Figure 9 shows the eddy diffusivity per RWB occurrence on the tropopause in the climate simulation (red lines), which is essentially a subset of what is shown in Figs. 5c,d. In the climate simulation, the mixing efficiency of CWB at higher latitudes is only slightly larger than that of AWB at lower latitudes (Figs. 9a,b). The difference in eddy diffusivity on the tropopause is much smaller than in the idealized life cycle simulations (not shown).

The composite frequencies of occurrence of the two types of RWB along the tropopause are shown in Fig. 10 with respect to jet latitude. As also shown in Fig. 9 (gray bars), AWB and CWB occur on two sides of the jet and there is little overlap. When the jet shifts poleward, AWB occurs more frequently while CWB occurs less frequently. Figures 11a and 11b show the eddy diffusivity across the tropopause and the contribution from RWB. As in the underworld, RWB contributes about half of the total eddy diffusivity and exhibits very similar meridional distribution compared to the total. Both the total and RWB eddy diffusivity peaks on the two flanks of jet, as a result of the combined effects of high mixing efficiency (Fig. 9) and high frequency (Fig. 10) linked to the RWB there. In terms of the variability associated with the jet shifting, a substantial portion of the total can be explained by the

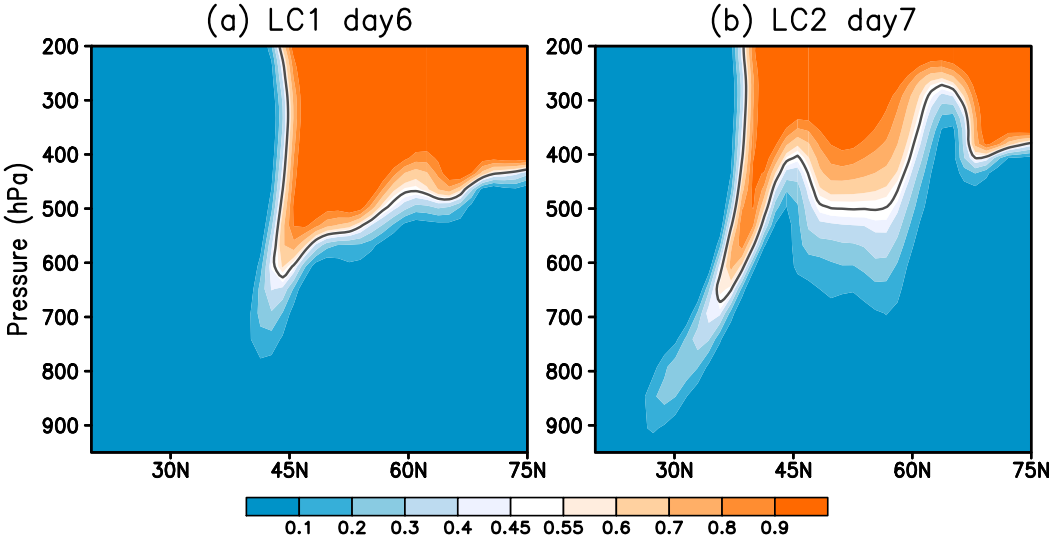

FIG. 8. Snapshots of stratospheric tracer concentration S (color shading) in the (a) LC1 and (b) LC2 idealized life cycle simulations on the day of maximum intensity. The gray solid line is $S = 0.5$ contour that represents the tropopause in the simulations.

RWB contribution (cf. Figs. 11a and 11b), which in turn is explained by the AWB and CWB frequency changes on the both sides of the jet (cf. Figs. 11c,d and 10a,b). On the poleward side of the jet, the eddy diffusivity across the tropopause weakens as the jet shifts poleward as a result of decreased CWB frequency. On the equatorward side of the jet, the eddy diffusivity increases as a result of increased AWB frequency. While AWB and CWB do exhibit different mixing efficiencies, these changes are predominantly explained by changes in RWB frequency itself.

c. *Section summary*

As the jet shifts poleward, the following occurs:

- upper-underworld eddy diffusivity decreases because of the difference in AWB and CWB mixing efficiencies.
- across the tropopause, eddy diffusivity decreases poleward of the jet because of decreased CWB frequency and increases equatorward of the jet because of increased AWB frequency.

6. Conclusions

A modified-Lagrangian-mean framework to quantify isentropic mixing is applied to Rossby wave breaking (RWB) in both free eddy life cycle simulations and a forced climate simulation. The focus of this study is

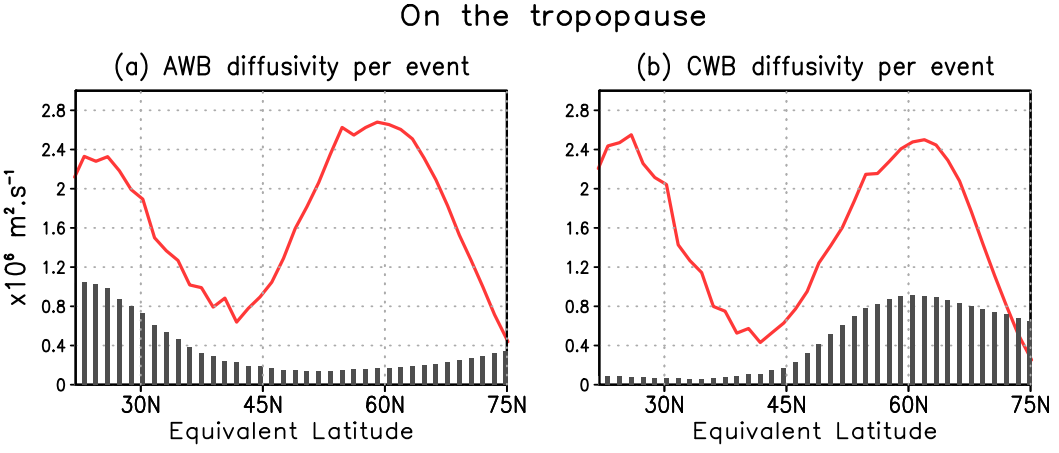

FIG. 9. Climatology of eddy diffusivity on the tropopause (red line) in the 25-yr climate simulation for (a) AWB and (b) CWB, normalized by their respective frequency of occurrence, denoted by gray bars.

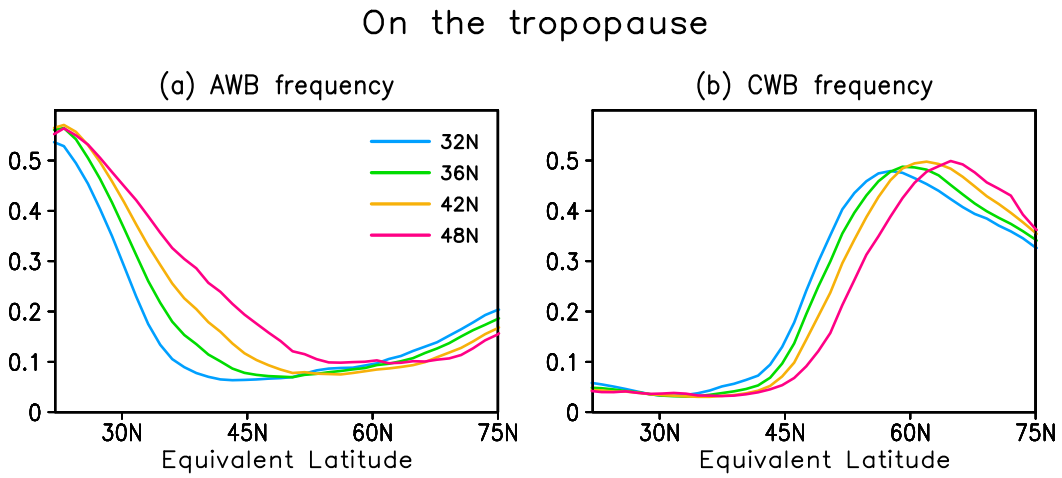

FIG. 10. Composite frequency of occurrence of Rossby wave breaking with respect to various jet positions for (a) AWB and (b) CWB along the dynamical tropopause. The jet latitudes are denoted in the legend in (a).

on the difference between the two flavors of RWB—anticyclonic wave breaking (AWB) and cyclonic wave breaking (CWB). It is found that in both sets of simulations and throughout different regions of the atmosphere, CWB has either comparable or stronger isentropic mixing efficiency than AWB. This result has

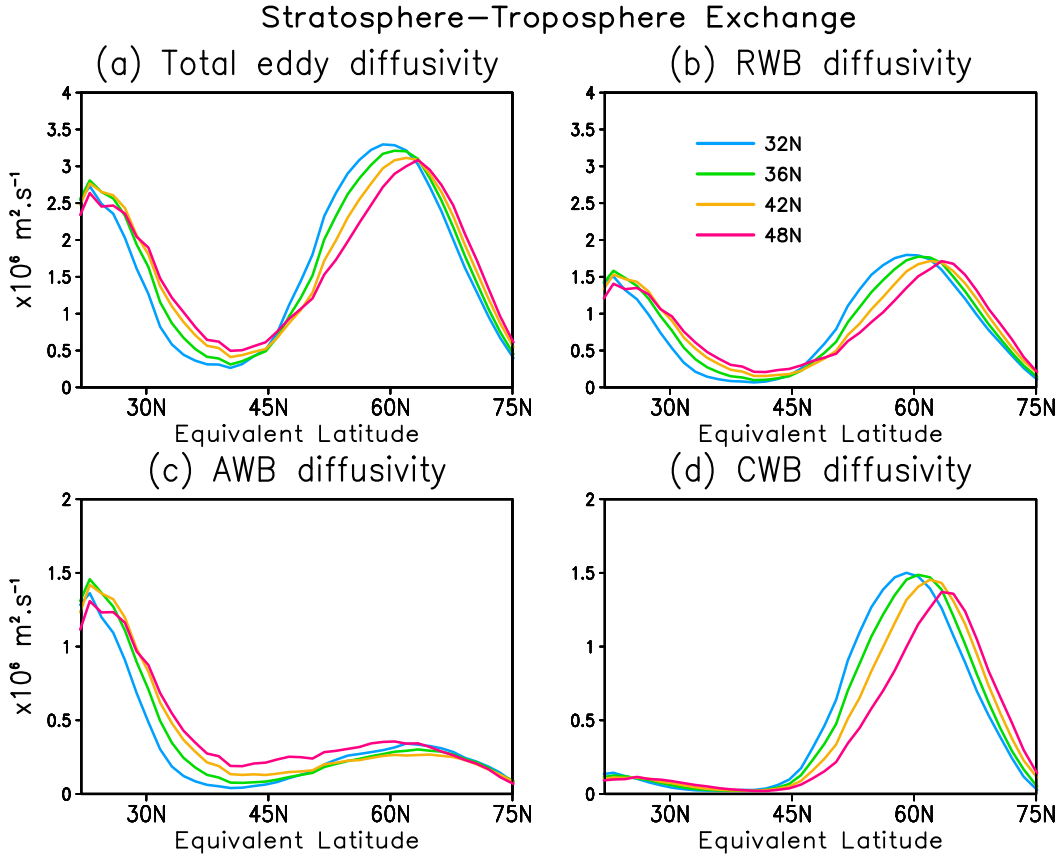

FIG. 11. Composite eddy diffusivity ($1 \times 10^6\,m^2\,s^{-1}$) along the dynamical tropopause with respect to various jet positions for the (a) total, (b) RWB, (c) AWB, and (d) CWB. The jet latitudes are denoted in the legend in (b).

implications for the influence of climate variability on isentropic mixing. In the upper underworld, since CWB occurs less frequently and AWB occurs more frequently as the jet shifts poleward, mixing differences translate into a decrease in total mixing strength (eddy diffusivity). Across the tropopause, AWB increases on the equatorward flank of the jet, leading to increased eddy diffusivity there. CWB decreased on the poleward flank of the jet, leading to decreased eddy diffusivity there.

In this study, we use an idealized dry dynamical core and the effect of moisture on isentropic mixing is neglected. According to (8), latent heat release by the phase change of moisture would directly affect the tracer distributions by cross-isentropic mass flux that, through continuity equation [see (5)], would affect the isentropic mixing. The exact influence of moisture on the isentropic mixing and the corresponding mechanisms are still unclear and warrant future research.

Although the simulations in this study are highly idealized, we argue that the conclusions obtained are applicable to the real atmosphere. Abalos et al. (2016) used ERA-Interim to show that in winter the effective diffusivity across the tropopause decreases in the mid- to high latitudes during a positive northern annular mode when the jet is more poleward, and increases during positive ENSO when the jet is more equatorward. These results are consistent with the modulation by the jet stream of the two types of RWB. Although our study does not directly address the jet shift in response to external forcing (e.g., anthropogenic climate change), we expect similar results to what is found here because of the same relationship between RWB and the jet stream in climate change simulations (e.g., Barnes and Polvani 2013). In fact, Orbe et al. (2015) demonstrated that isentropic mixing from the midlatitude boundary layer to the Arctic increases over the northeast Pacific with climate change in a state-of-the-art GCM where the jet stream shifts equatorward. This is consistent with our argument that an equatorward jet shift increases the frequency of the more efficient cyclonic wave breaking, and thus, increases the midlatitude mixing strength.

In the real atmosphere, certain constituents whose spatial distributions are impacted by climate change also contribute to the climate forcing. Examples include carbon dioxide, ozone, various species of aerosols, and water vapor. Thus, understanding the passive response of atmospheric constituents to climate change is an important step toward understanding the entire feedback loop. This study provides a mechanistic explanation for how the isentropic mixing of constituents may respond to future jet shifts.

Acknowledgments. This work was supported by the Climate and Large-scale Dynamics Program of the National Science Foundation under Grant 1419818. We thank three anonymous reviewers for their thoughtful and constructive comments that significantly improved this manuscript.

APPENDIX

Derivation of Effective Diffusivity

Instead of assuming that

$$\dot{q} = \kappa\nabla^2 q = \kappa\nabla\cdot\nabla q, \tag{A1}$$

we assume a more general form of hyperdiffusion for 2D flow:

$$\dot{q} = \kappa\nabla^{2m} q = \kappa\nabla\cdot\nabla[\nabla^{2(m-1)} q], \tag{A2}$$

where (A1) is the special case in which $m = 1$. Inserting (A2) into $\mathcal{M}\{\dot{q}\}$ leads to

$$\mathcal{M}\{\dot{q}\} = \sigma_0\kappa\iint_{q^*\le q}\nabla\cdot\nabla[\nabla^{2(m-1)} q^*]\,dA.$$

Using the divergence theorem,

$$\mathcal{M}\{\dot{q}\} = \sigma_0\kappa\oint_{q^*=q}\nabla[\nabla^{2(m-1)} q^*]\cdot\frac{\nabla q^*}{|\nabla q^*|}\,dl,$$

and using the relation,

$$\frac{\partial\mathcal{M}\{\,\}}{\partial q} = \sigma_0\oint_q\frac{\{\,\}}{|\nabla_\theta q^*|}\,dl,$$

one obtains

$$\begin{aligned}\mathcal{M}\{\dot{q}\} &= \sigma_0\kappa\frac{\partial}{\partial q}\iint\nabla[\nabla^{2(m-1)} q^*]\cdot\nabla q^* dA\\ &= \sigma_0\kappa\frac{\partial}{\partial A}\iint\nabla[\nabla^{2(m-1)} q^*]\cdot\nabla q^*\,dA\,\frac{\partial A}{\partial q}\\ &= \sigma_0\kappa\underbrace{\frac{\dfrac{\partial}{\partial A}\iint\nabla[\nabla^{2(m-1)} q^*]\cdot\nabla q^*\,dA}{\left(\dfrac{\partial q}{\partial A}\right)^2}}_{L_{\rm eq}^2}\frac{\partial q}{\partial A}.\end{aligned} \tag{A3}$$

This form of effective diffusivity $\kappa_{\rm eff}$ is identical to that in Nakamura and Zhu (2010, their appendix D). Letting

$m = 1$, L_{eq}^2 takes the form of (10), which is identical to that in Nakamura (1996).

REFERENCES

Abalos, M., B. Legras, and E. Shuckburgh, 2016: Interannual variability in effective diffusivity in the upper troposphere/lower stratosphere from reanalysis data. *Quart. J. Roy. Meteor. Soc.*, **142**, 1847–1861, https://doi.org/10.1002/qj.2779.

Appenzeller, C., and H. Davies, 1992: Structure of stratospheric intrusions into the troposphere. *Nature*, **358**, 570–572, https://doi.org/10.1038/358570a0.

——, ——, and W. Norton, 1996: Fragmentation of stratospheric intrusions. *J. Geophys. Res.*, **101**, 1435–1456, https://doi.org/10.1029/95JD02674.

Barnes, E. A., and D. L. Hartmann, 2010: Influence of eddy-driven jet latitude on North Atlantic jet persistence and blocking frequency in CMIP3 integrations. *Geophys. Res. Lett.*, **37**, L23802, https://doi.org/10.1029/2010GL045700.

——, and ——, 2012: Detection of Rossby wave breaking and its response to shifts of the midlatitude jet with climate change. *J. Geophys. Res.*, **117**, D09117, https://doi.org/10.1029/2012JD017469.

——, and L. Polvani, 2013: Response of the midlatitude jets, and of their variability, to increased greenhouse gases in the CMIP5 models. *J. Climate*, **26**, 7117–7135, https://doi.org/10.1175/JCLI-D-12-00536.1.

Barrie, L. A., 1986: Arctic air pollution: An overview of current knowledge. *Atmos. Environ.*, **20**, 643–663, https://doi.org/10.1016/0004-6981(86)90180-0.

Butchart, N., and E. E. Remsberg, 1986: The area of the stratospheric polar vortex as a diagnostic for tracer transport on an isentropic surface. *J. Atmos. Sci.*, **43**, 1319–1339, https://doi.org/10.1175/1520-0469(1986)043<1319:TAOTSP>2.0.CO;2.

Butler, A. H., D. W. Thompson, and R. Heikes, 2010: The steady-state atmospheric circulation response to climate change–like thermal forcings in a simple general circulation model. *J. Climate*, **23**, 3474–3496, https://doi.org/10.1175/2010JCLI3228.1.

Chen, G., and A. Plumb, 2014: Effective isentropic diffusivity of tropospheric transport. *J. Atmos. Sci.*, **71**, 3499–3520, https://doi.org/10.1175/JAS-D-13-0333.1.

Chen, P., 1995: Isentropic cross-tropopause mass exchange in the extratropics. *J. Geophys. Res.*, **100**, 16 661–16 673, https://doi.org/10.1029/95JD01264.

Chen, W. Y., and H. M. Van den Dool, 1999: Significant change of extratropical natural variability and potential predictability associated with the El Nino/Southern Oscillation. *Tellus*, **51A**, 790–802, https://doi.org/10.3402/tellusa.v51i5.14493.

Eckhardt, S., A. Stohl, H. Wernli, P. James, C. Forster, and N. Spichtinger, 2004: A 15-year climatology of warm conveyor belts. *J. Climate*, **17**, 218–237, https://doi.org/10.1175/1520-0442(2004)017<0218:AYCOWC>2.0.CO;2.

Edouard, S., R. Vautard, and G. Brunet, 1997: On the maintenance of potential vorticity in isentropic coordinates. *Quart. J. Roy. Meteor. Soc.*, **123**, 2069–2094, https://doi.org/10.1002/qj.49712354314.

Haynes, P., and E. Shuckburgh, 2000a: Effective diffusivity as a diagnostic of atmospheric transport: 1. Stratosphere. *J. Geophys. Res.*, **105**, 22 777–22 794, https://doi.org/10.1029/2000JD900093.

——, and ——, 2000b: Effective diffusivity as a diagnostic of atmospheric transport: 2. Troposphere and lower stratosphere. *J. Geophys. Res.*, **105**, 22 795–22 810, https://doi.org/10.1029/2000JD900092.

Held, I. M., and M. J. Suarez, 1994: A proposal for the intercomparison of the dynamical cores of atmospheric general circulation models. *Bull. Amer. Meteor. Soc.*, **75**, 1825–1830, https://doi.org/10.1175/1520-0477(1994)075<1825:APFTIO>2.0.CO;2.

Holton, J. R., P. H. Haynes, M. E. McIntyre, A. R. Douglass, R. B. Rood, and L. Pfister, 1995: Stratosphere-troposphere exchange. *Rev. Geophys.*, **33**, 403–439, https://doi.org/10.1029/95RG02097.

Hoskins, B. J., 1991: Towards a PV-θ view of the general circulation. *Tellus*, **43A**, 27–35, https://doi.org/10.3402/tellusa.v43i4.11936.

Jing, P., D. Cunnold, H. Wang, and E. Yang, 2004: Isentropic cross-tropopause ozone transport in the Northern Hemisphere. *J. Atmos. Sci.*, **61**, 1068–1078, https://doi.org/10.1175/1520-0469(2004)061<1068:ICOTIT>2.0.CO;2.

Leibensperger, E. M., and R. A. Plumb, 2014: Effective diffusivity in baroclinic flow. *J. Atmos. Sci.*, **71**, 972–984, https://doi.org/10.1175/JAS-D-13-0217.1.

Lelieveld, J., and F. J. Dentener, 2000: What controls tropospheric ozone? *J. Geophys. Res.*, **105**, 3531–3551, https://doi.org/10.1029/1999JD901011.

Lippmann, M., 1989: Health effects of ozone: A critical review. *J. Air Waste Manage. Assoc.*, **39**, 672–695, https://doi.org/10.1080/08940630.1989.10466554.

Liu, C., and E. A. Barnes, 2015: Extreme moisture transport into the Arctic linked to Rossby wave breaking. *J. Geophys. Res. Atmos.*, **120**, 3774–3788, https://doi.org/10.1002/2014JD022796.

——, and ——, 2018: Synoptic formation of double tropopauses. *J. Geophys. Res. Atmos.*, **123**, 693–707, https://doi.org/10.1002/2017JD027941.

——, X. Ren, and X. Yang, 2014: Mean flow-storm track relationship and Rossby wave breaking in two types of El-Niño. *Adv. Atmos. Sci.*, **31**, 197–210, https://doi.org/10.1007/s00376-013-2297-7.

Madonna, E., H. Wernli, H. Joos, and O. Martius, 2014: Warm conveyor belts in the ERA-Interim dataset (1979–2010). Part I: Climatology and potential vorticity evolution. *J. Climate*, **27**, 3–26, https://doi.org/10.1175/JCLI-D-12-00720.1.

McIntyre, M., 1980: Towards a Lagrangian-mean description of stratospheric circulations and chemical transports. *Philos. Trans. Roy. Soc. London*, **296**, 129–148, https://doi.org/10.1098/rsta.1980.0160.

Nakamura, N., 1995: Modified Lagrangian-mean diagnostics of the stratospheric polar vortices. Part I: Formulation and analysis of GFDL SKYHI GCM. *J. Atmos. Sci.*, **52**, 2096–2108, https://doi.org/10.1175/1520-0469(1995)052<2096:MLMDOT>2.0.CO;2.

——, 1996: Two-dimensional mixing, edge formation, and permeability diagnosed in an area coordinate. *J. Atmos. Sci.*, **53**, 1524–1537, https://doi.org/10.1175/1520-0469(1996)053<1524:TDMEFA>2.0.CO;2.

——, 2004: Quantifying asymmetric wave breaking and two-way transport. *J. Atmos. Sci.*, **61**, 2735–2748, https://doi.org/10.1175/JAS3296.1.

——, and D. Zhu, 2010: Finite-amplitude wave activity and diffusive flux of potential vorticity in eddy–mean flow interaction. *J. Atmos. Sci.*, **67**, 2701–2716, https://doi.org/10.1175/2010JAS3432.1.

Orbe, C., P. A. Newman, D. W. Waugh, M. Holzer, L. D. Oman, F. Li, and L. M. Polvani, 2015: Air-mass origin in the Arctic. Part II: Response to increases in greenhouse gases. *J. Climate*, **28**, 9105–9120, https://doi.org/10.1175/JCLI-D-15-0296.1.

Pan, L. L., and Coauthors, 2009: Tropospheric intrusions associated with the secondary tropopause. *J. Geophys. Res.*, **114**, D10302, https://doi.org/10.1029/2008JD011374.

Plumb, R., and J. Mahlman, 1987: The zonally averaged transport characteristics of the GFDL general circulation/transport model. *J. Atmos. Sci.*, **44**, 298–327, https://doi.org/10.1175/1520-0469(1987)044<0298:TZATCO>2.0.CO;2.

Polvani, L. M., and J. G. Esler, 2007: Transport and mixing of chemical air masses in idealized baroclinic life cycles. *J. Geophys. Res.*, **112**, D23102, https://doi.org/10.1029/2007JD008555.

Raatz, W. E., and G. E. Shaw, 1984: Long-range tropospheric transport of pollution aerosols into the Alaskan arctic. *J. Climate Appl. Meteor.*, **23**, 1052–1064, https://doi.org/10.1175/1520-0450(1984)023<1052:LRTTOP>2.0.CO;2.

Randel, W. J., D. J. Seidel, and L. L. Pan, 2007: Observational characteristics of double tropopauses. *J. Geophys. Res.*, **112**, D07309, https://doi.org/10.1029/2006JD007904.

Rasmusson, E. M., and J. M. Wallace, 1983: Meteorological aspects of the El Niño/Southern Oscillation. *Science*, **222**, 1195–1202, https://doi.org/10.1126/science.222.4629.1195.

Ren, X., Y. Zhang, and Y. Xiang, 2008: Connections between wintertime jet stream variability, oceanic surface heating, and transient eddy activity in the North Pacific. *J. Geophys. Res.*, **113**, D21119, https://doi.org/10.1029/2007JD009464.

Rivière, G., 2011: A dynamical interpretation of the poleward shift of the jet streams in global warming scenarios. *J. Atmos. Sci.*, **68**, 1253–1272, https://doi.org/10.1175/2011JAS3641.1.

Shapiro, M., 1980: Turbulent mixing within tropopause folds as a mechanism for the exchange of chemical constituents between the stratosphere and troposphere. *J. Atmos. Sci.*, **37**, 994–1004, https://doi.org/10.1175/1520-0469(1980)037<0994:TMWTFA>2.0.CO;2.

Shaw, N., and E. Austin, 1930: *The Physical Processes of Weather.* Vol. 3, *Manual of Meteorology*, Cambridge University Press, 474 pp.

Škerlak, B., M. Sprenger, and H. Wernli, 2014: A global climatology of stratosphere-troposphere exchange using the ERA-Interim data set from 1979 to 2011. *Atmos. Chem. Phys.*, **14**, 913–937, https://doi.org/10.5194/acp-14-913-2014.

Sprenger, M., and H. Wernli, 2003: A northern hemispheric climatology of cross-tropopause exchange for the ERA15 time period (1979–1993). *J. Geophys. Res.*, **108**, 8521, doi:10.1029/2002JD002636.

Strong, C., and G. Magnusdottir, 2008: Tropospheric Rossby wave breaking and the NAO/NAM. *J. Atmos. Sci.*, **65**, 2861–2876, https://doi.org/10.1175/2008JAS2632.1.

Thompson, D. W., and S. Solomon, 2002: Interpretation of recent Southern Hemisphere climate change. *Science*, **296**, 895–899, https://doi.org/10.1126/science.1069270.

Thorncroft, C., B. Hoskins, and M. McIntyre, 1993: Two paradigms of baroclinic-wave life-cycle behaviour. *Quart. J. Roy. Meteor. Soc.*, **119**, 17–55, https://doi.org/10.1002/qj.49711950903.

Trepte, C. R., R. E. Veiga, and M. P. McCormick, 1993: The poleward dispersal of Mount Pinatubo volcanic aerosol. *J. Geophys. Res.*, **98**, 18 563–18 573, https://doi.org/10.1029/93JD01362.

Walker, C. C., and T. Schneider, 2006: Eddy influences on Hadley circulations: Simulations with an idealized GCM. *J. Atmos. Sci.*, **63**, 3333–3350, https://doi.org/10.1175/JAS3821.1.

Wang, S., and L. M. Polvani, 2011: Double tropopause formation in idealized baroclinic life cycles: The key role of an initial tropopause inversion layer. *J. Geophys. Res.*, **116**, D05108, https://doi.org/10.1029/2010JD015118.

Woollings, T., B. Hoskins, M. Blackburn, and P. Berrisford, 2008: A new Rossby wave-breaking interpretation of the North Atlantic Oscillation. *J. Atmos. Sci.*, **65**, 609–626, https://doi.org/10.1175/2007JAS2347.1.

——, A. Hannachi, and B. Hoskins, 2010: Variability of the North Atlantic eddy-driven jet stream. *Quart. J. Roy. Meteor. Soc.*, **136**, 856–868, https://doi.org/10.1002/qj.625.